

Downslope Flows on a Low-Angle Slope and Their Interactions with Valley Inversions. Part II: Numerical Modeling

SHIYUAN ZHONG

Department of Geography, Michigan State University, East Lansing, Michigan

C. DAVID WHITEMAN*

Department of Meteorology, University of Utah, Salt Lake City, Utah

(Manuscript received 18 December 2006, in final form 7 September 2007)

ABSTRACT

The characteristics of well-developed downslope winds observed by tethered balloon soundings at multiple locations over a low-angle slope in the Salt Lake Valley are studied using the Regional Atmospheric Modeling System (RAMS). The model successfully simulated the key properties of the observed wind and temperature structure and evolution and provided insight into the forcing mechanisms. The results show that, although the slope angle is only 1.6° , the buoyancy force associated with the local temperature perturbation caused by nocturnal cooling of the slope surface is capable of producing the unusually strong and deep downslope winds observed by the tethersondes. The hypothesis that the flow is produced locally by the temperature deficit is further confirmed by analysis of the momentum budget that indicates a very small contribution from advection to the downslope mass flux. The analysis also reveals the importance of the along-slope pressure gradient force, which has been neglected by some previous investigators. On an isolated slope, the pressure gradient force, which develops as the downslope-flow layer deepens with downslope distance, is important mostly in the upper part of the downslope wind layer where it counterbalances the buoyancy force. On a slope in a valley, the pressure gradient force interacts with the valley inversion to produce intermittency in the downslope jet and may also significantly slow the flow as the inversion strengthens during the night. The simulations for two different observational nights indicate that the maximum downslope wind speed is sensitive to ambient stability, with near-neutral ambient stability yielding a stronger downslope jet than does a more stable ambient atmosphere. Sensitivity studies suggest that an increase in down-valley winds leads to a decrease in the maximum downslope wind speed and an increase in the thickness of the downslope wind layer. An increase in slope roughness, on the other hand, increases the height of the downslope jet but has little effect on other properties. The downslope wind is stronger over a gentle 1.6° slope than over a much steeper slope of 11° , mainly because of the combination of the stronger buoyancy and weaker pressure gradient over the gentle slope.

1. Introduction

Most mountain slopes experience nocturnal downslope or drainage flows on clear nights with weak ambient winds. The characteristics of the drainage flows, however, vary widely depending on factors such as slope angle, slope surface characteristics, and ambient

wind and stability [see the review by Poulos (1997)]. These drainage flows can be important for atmospheric transport, dispersion, and deposition within mountain valleys. Because the drainage flows on the valley side slopes can influence the structure of the valley boundary layer, they may also affect the valley winds at night. The nocturnal drainage flows from slopes can sometimes pool up in basins or in valleys that are not well ventilated at night, leading to persistent air pollution episodes (Whiteman et al. 2001).

Many previous investigations have examined the mechanisms and characteristics of nocturnal drainage flows by means of analytical solutions (Fleagle 1950; Defant 1949; Manins and Sawford 1979a,b; Gutman

* Certified Consulting Meteorologist (CCM)

Corresponding author address: Dr. Shiyuan (Sharon) Zhong, Department of Geography, Michigan State University, East Lansing, MI 48824.
E-mail: zhongs@msu.edu

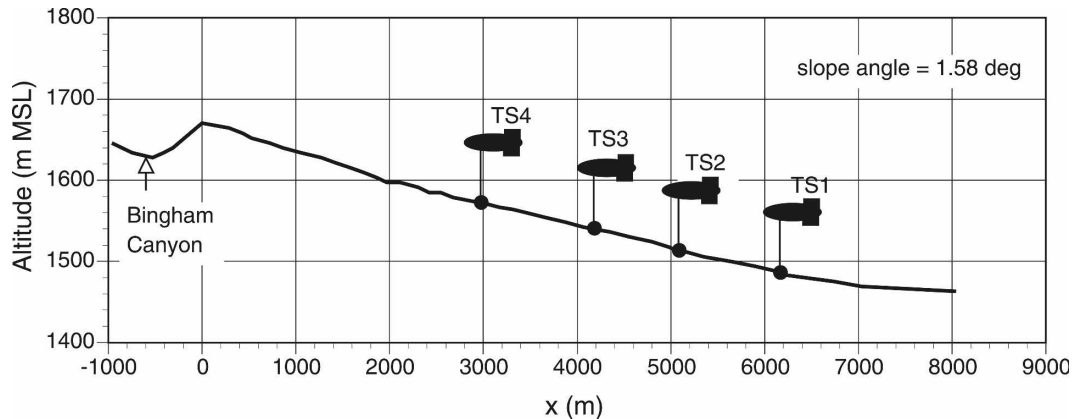


FIG. 1. Topographic cross section of the low-angle slope showing the instrument locations. The cross section is drawn through the line of tethersondes and then northwestward up the terrain gradient from TS4 to the ridge on the east side of Bingham Canyon.

1983; Haiden and Whiteman 2005), numerical models (Petkovsek and Hocevar 1971; Fitzjarrald 1984; McNider and Pielke 1984; Kondo and Sato 1988; Bossert and Poulos 1995; Skillingstad 2003; Smith and Skillingstad 2005), laboratory experiments (Monti et al. 2002; Hunt et al. 2003), and field observations (Orgill and Schreck 1985; Clements et al. 1989; Doran and Horst 1981; Mahrt et al. 2001). While numerical modeling of downslope flows has made significant progress with increased horizontal and vertical resolutions that allow the capturing of shallow drainage flows developed over real topography, the proliferation of numerical models has not been matched by a corresponding increase in observational studies. Specialized downslope-flow datasets have been largely unavailable to answer scientific questions about the down-slope flows for the typical ranges of internal (slope angle, roughness, sensible heat flux, and radiative flux divergence) and external (winds above the slope layer and ambient stability) parameters. Existing datasets on nocturnal drainage flows are mostly limited to near-surface observations using short towers. Recent advances in boundary layer wind and temperature profiling using remote sensing instruments (such as radar wind profilers and sodars) have not helped to improve slope-flow observations because the lowest range gates of these instruments are too high (~ 120 m for a profiler and at least 10 m for a minisodar) to resolve the shallow downslope-flow layer.

In October of 2000, a slope-flow experiment was conducted as part of the U.S. Department of Energy's Vertical Transport and Mixing experiment (VTMX; Doran et al. 2002) in Utah's Salt Lake Valley. Detailed observations of nocturnal downslope flows developed on a relatively uniform, low-angle ($\sim 1.6^\circ$) slope were ob-

tained using a line of four tethered balloons located about 1 km apart from the top to the bottom of the slope on the southwest side of the Salt Lake Valley. The simultaneous observations of the wind and temperature profiles from the tethersondes at four locations along the slope provided rare details of the dynamical and thermal structure of slope flows. The design of the slope experiment and the results from the observations were presented in Whiteman and Zhong (2008, hereinafter Part I). The current paper describes the numerical simulations designed to shed light on the observations and provide insight into the mechanisms that drive the strong slope flows and govern their evolution. Section 2 briefly describes observations, and section 3 describes the numerical model configuration and design of the numerical simulations. The results of the model simulations and analyses are given in section 4. Conclusions appear in section 5.

2. The observations

This section briefly summarizes the observations that are relevant to this study. For details on the slope-flow experiment and the observations, refer to Haiden and Whiteman (2005) and Part I. The site for the slope-flow experiment was a smooth, uniform, low-angle ($\sim 1.6^\circ$) slope in the southwestern part of the Salt Lake Valley. Figure 1 is the topographic cross section of the slope on which four tethered balloons were operated during the experiment to collect data on slope flows and their along-slope variation. The tethersonde ("sonde") sites, TS1, TS2, TS3, and TS4, are numbered from the lowest to the highest altitudes—1485, 1513, 1539, and 1572 m MSL, respectively—and they are approximately 1 km apart. Frequent soundings were made concu-

rently on clear nights to heights of 200–300 m. Occasional deeper ascents to approximately 450 m were made at TS1 to sample the valley atmosphere above the slope boundary layer. The sondes measured pressure, temperature, relative humidity, wind speed, and wind direction.

The tethersonde observations show that downslope flows were initiated as the slope went into shadow just before astronomical sunset when the surface sensible heat flux changed sign. They accelerated after their initiation, attaining a more or less steady state in mid-evening, but weakened and became intermittent later in the night. The observed downslope flows were typically 100–150 m deep with a peak speed of 5–6 m s⁻¹ occurring at 10–15 m above the slope surface. There were some variations from night to night in the downslope development of the wind and temperature structure. The temperature deficit above the slope, the strength of the downslope jet, and its height above the ground generally increased with downslope distance. The wind speed increase from site to site with downslope distance was seen not only at the height of the jet maximum but also through the entire depth of the downslope flow.

The downslope flows observed by the tethersondes were much stronger and deeper than were anticipated for a low-angle slope. The downslope flows began to develop at approximately the same time at all four sites and evolved mostly uniformly with time, rather than appearing as a sudden wind pulse shortly after sunset and moving from upper slope to lower slope. In addition, the vertical profiles of wind speed and temperature were similar in shape at the four observational sites. These observations led to the hypothesis that the slope flow was in local equilibrium and was driven by local forcing. Numerical model simulations were performed to test this hypothesis and to help to explain why the observed slope flows were stronger and deeper than those previously observed over steeper slopes on isolated mountainsides and what role the ambient inversion that built up in the valley played in the downslope flow evolution.

3. Model configuration and numerical simulations

The Regional Atmospheric Modeling System (RAMS; Pielke et al. 1992) is used for the model simulations. RAMS is a primitive equation, nonhydrostatic model based on a terrain-following coordinate system. RAMS contains various options for describing physical processes. Those selected for this study include a level-2.5 subgrid-scale turbulent parameterization scheme (Mellor and Yamada 1982) with a prognostic equation for

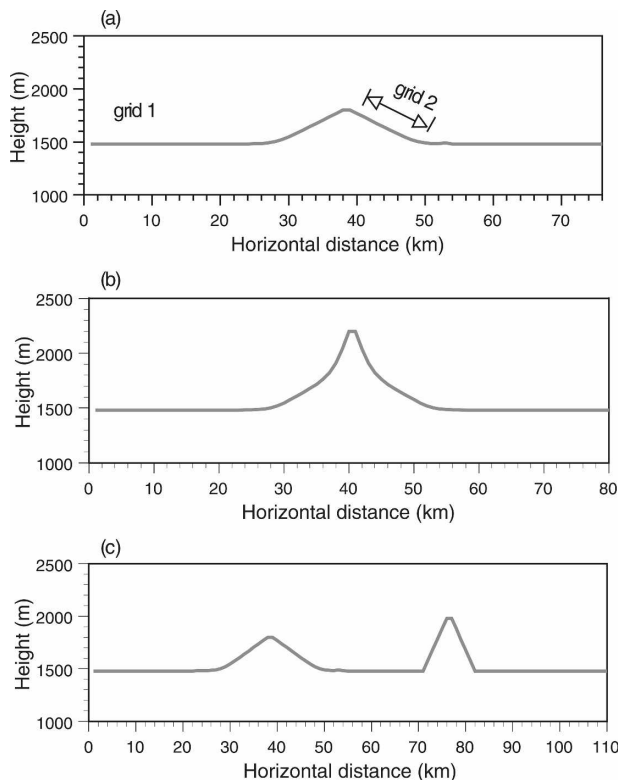


FIG. 2. Topography cross sections used in the simulations, as described in the text.

turbulent kinetic energy, the Louis (1979) formulation for surface layer parameterization, the Tremback and Kessler (1985) multilayer soil model to predict diurnal variations in soil temperature and moisture, and the Chen and Cotton (1983) cloud radiation schemes for the longwave and shortwave radiative transfer.

RAMS simulations are performed using three different terrain cross sections as shown in Fig. 2. The first terrain cross section (Fig. 2a) is a single hill composed of two symmetric slopes of 1.6° slope angle, similar to the slope where the tethersonde observations were made. This terrain cross section is designed to investigate whether a uniform gentle slope with such a low slope angle is capable of producing downslope flows that are as deep and strong as the observed slope flows and what mechanisms are responsible for the development and evolution of the slope flows. The second terrain cross section (Fig. 2b) is designed to estimate the contribution from the waste-rock pile immediately upwind of the gentle slope to the mass and momentum fluxes associated with the downslope winds observed over the gentle slope. Based on the actual topography, the waste-rock pile, which is immediately upwind of the 1.6° gentle slope, has a slope angle of approximately 13° and a length of about 2 km. This terrain cross section

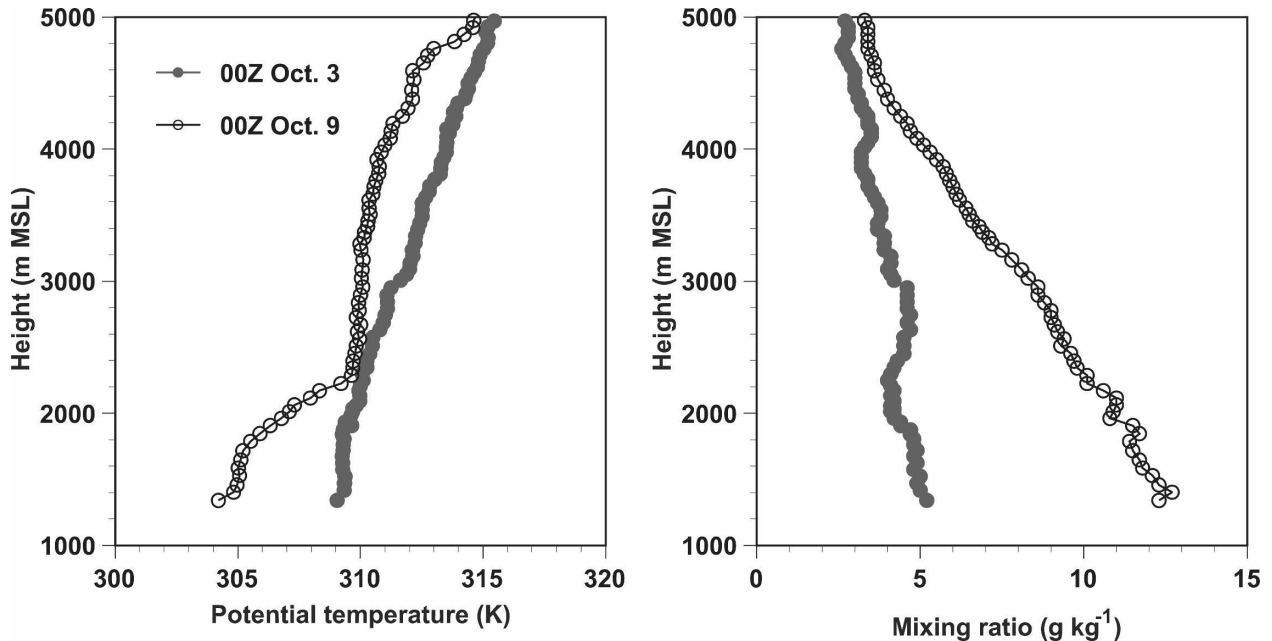


FIG. 3. The 0000 UTC radiosonde sounding profiles of (left) potential temperature and (right) mixing ratio on 3 and 9 Oct 2000 that were used to initialize the simulations.

will further test the hypothesis that the observed downslope flow is produced by local forcing. The third terrain cross section (Fig. 2c) is composed of two hills separated by a valley that is 20 km wide. This terrain cross section, which resembles the actual terrain cross section in the southern part of the Salt Lake Valley where the observations took place, allows an examination of the effect of the valley inversion on the development of downslope flows. The existence of the valley allows cold air draining down the mountain slopes to accumulate and an inversion to build up from the valley floor during the course of the night; this cross section is used to investigate the interaction of slope flows with the valley inversion. The asymmetry of the cross section with a gentle slope (1.6°) on one side and a steep slope (11°) on the other enables a comparison of flow development on the two slopes under the same ambient conditions, providing insight into why the observed slope flows over a gentle slope are stronger and deeper than those previously reported from observations made over steeper slopes.

For each terrain cross section, two nested grids are employed. The coarse grid, which has a horizontal grid spacing of 1000 m, covers the entire terrain cross section shown in Fig. 2. To better resolve the downslope flows and their along-slope variation, a fine grid with a grid spacing of 250 m is placed over the portion of the gentle slope where the tethered balloon data were collected. The 250-m horizontal resolution is necessary to resolve

the 1000-m distance between two tethered balloon sites, and the coarse grid allows the effects of lateral boundaries on the slope of interest to be minimized. To capture the shallow slope winds that usually peak at 10–15 m above the slope surface, fine vertical resolution is employed with 15 vertical levels within the lowest 50 m and 6 within the lowest 15 m (at 1, 3.1, 5.3, 7.7, 10.3, and 13.2 m). The grid is gradually stretched to 1000 m at the model top at about 10 km.

Simulations were performed to simulate conditions found during several intensive observational periods (IOPs). For each simulation, zero background wind was assumed and the temperature and moisture were initialized using a radiosonde sounding taken at 1600 MST from Wheeler Farm, which is located near the center of the valley approximately 2000 m northeast of the slope experiment site and is considered most representative of the valley atmosphere.

4. Results and discussions

a. Characteristics of downslope flows

This section discusses the results from the simulations using the first terrain cross section—in particular, simulations are made for the two intensive observational periods, IOP 1 on 2 October and IOP 4 on 8 October 2000, when the tethered balloon soundings observed well-developed downslope winds. Figure 3

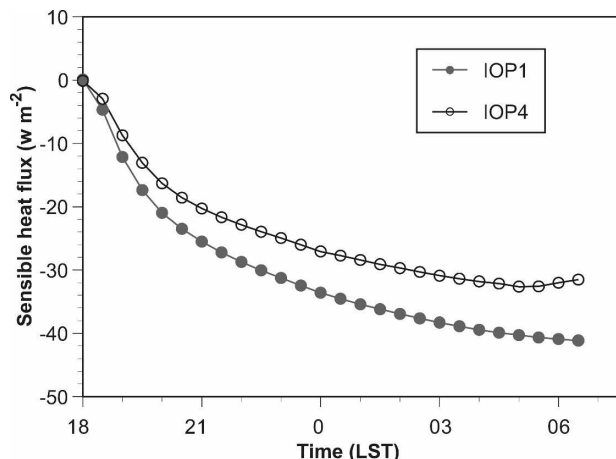


FIG. 4. The time series of the simulated sensible heat flux during the nights of IOP 1 on 2–3 Oct and IOP 4 on 8–9 Oct 2000 at the TS1 site.

shows the initial profiles of potential temperature and mixing ratio at 0000 UTC [1700 mountain standard time (MST)] in the afternoon on each of the two IOP days. The atmospheric conditions for IOP 1 were much drier and warmer than for IOP 4. The mixing ratio within the valley atmosphere was about 5 g kg^{-1} for IOP 1 and $11\text{--}13 \text{ g kg}^{-1}$ for IOP 4. The dry conditions during IOP 1 corresponded to a warmer atmosphere with a potential temperature in the lowest 1 km about 5 K higher on average than the potential temperature at the same time in the afternoon of IOP 4. In addition, a near-neutral stratification existed in the valley atmosphere during IOP 1, whereas the valley atmosphere was stable during IOP 4 as indicated by an increase of potential temperature of about 5 K from the valley floor to 1 km AGL.

Despite different initial ambient atmospheric conditions, simulations on both nights developed a downslope flow shortly after sunset when the ground surface began to cool as a result of longwave radiation loss. Figure 4 shows time series of simulated sensible heat flux at the TS1 site. The sunset times for IOP 1 on 2 October and IOP 4 on 8 October were 1907 and 1857 MST, respectively. However in both cases, the surface sensible heat fluxes became negative about an hour before sunset when net longwave radiation loss first exceeded net solar radiation gain. The downward sensible heat fluxes continued to increase throughout the night because of the increase of near-surface drainage winds.

Comparisons of simulated and observed profiles of downslope wind component and potential temperature at tethered sites TS1, TS2, and TS3 are shown in Figs. 5 and 6 for the two IOPs. On both nights, the

model simulations adequately reproduced key features of the observed structure and evolution of the downslope flow and the temperature inversion.

In IOP 1, the observed downslope jet at 1945 MST occurred at 16, 22, and 20 m above the surface at TS1, TS2, and TS3, respectively, which was slightly below the height of the nocturnal surface-based inversion at about 25 m AGL. The jet speed increased in the downslope direction from 4.9 m s^{-1} at TS3 to 5.8 m s^{-1} at TS2 to 6.2 m s^{-1} at TS1. Although the height of the jet did not change much, the jet speed increased by about 1 m s^{-1} at 2120 MST to 5.9, 6.8, and 7.1 m s^{-1} . The simulation captured the observed increase in jet speed with time and with downslope distance, but the simulated maximum wind speed was about 1 m s^{-1} weaker and the jet height was 5–10 m higher than was observed at the three sites. The simulated jet was also broader than the observed jet; in other words, the decrease of the wind speed above the nose of the jet was not as rapid as in the observations. The higher jet nose and the broader profile may be attributed to the simulated inversion being slightly weaker and deeper than the observed inversion.

In a similar way, for IOP 4 the simulated jet is also at a slightly higher level and is somewhat broader than was observed, but the maximum jet speed matches the observed speed very well without the underprediction seen in IOP 1. On this night, the observed inversion was shallower than during IOP 1, which makes the discrepancy between the simulated and the observed temperature inversion slightly larger. The modeled inversion is weaker and deeper. Previous studies (e.g., Zhong and Fast 2003) have attributed similar differences found between simulated and observed lower boundary layer wind and temperature structure over complex terrain to the lack of vertical resolution. Inadequate vertical resolution is, however, unlikely to be the case here because of the very fine vertical resolution used in the lowest 50 m (1, 3.1, 5.3, 7.7, 10.3, 13.2, 16.2, 19.5, 23.1, 26.9, 31.1, 35.6, 40.4, and 51.3 m) for these simulations.

Although the basic characteristics of the observed downslope winds, such as the vertical structure, along-slope variation, and time variation, are similar on the two nights, the maximum jet speed is $1\text{--}2 \text{ m s}^{-1}$ stronger during IOP 1 than during IOP 4. As shown by the initial potential temperature profiles from the radiosonde soundings in Fig. 3, the ambient atmosphere is near neutral for IOP 1 whereas it was stable for IOP 4. The tethered potential temperature profiles shown in Figs. 5 and 6 further confirm this difference in ambient stability. The simulations of the two IOPs successfully

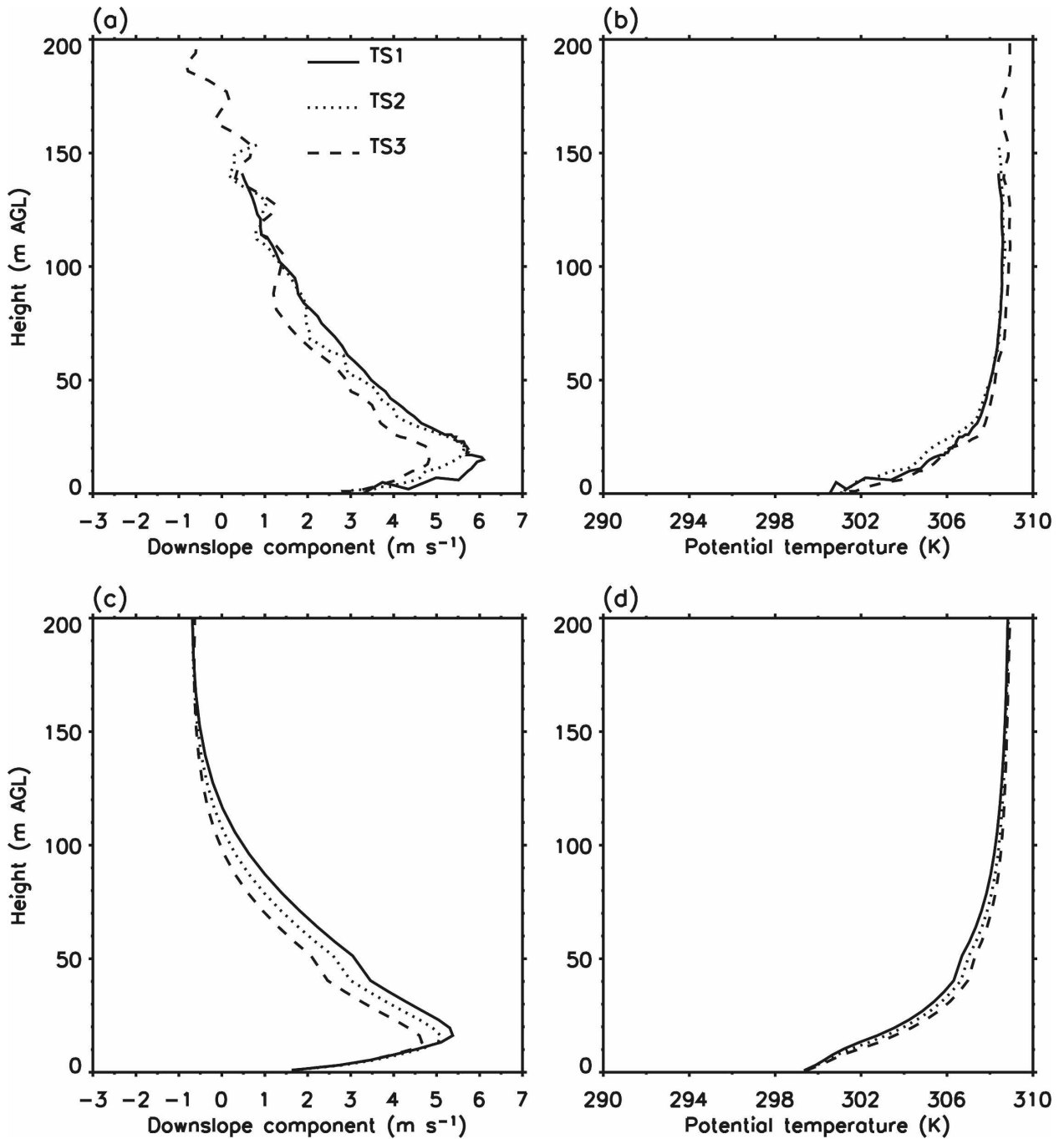


FIG. 5. Profiles of downslope wind speed and potential temperature at TS1, TS2, and TS3 during IOP 1 on the evening of 2 Oct 2000 at (a)–(d) 1945 and (e)–(h) 2120 MST. Observed profiles are shown in (a), (b), (e), and (f), and simulated profiles are shown in (c), (d), (g), and (h).

reproduced these differences in wind and potential temperature profiles. Because the two simulations differ only by the initial thermodynamic profiles shown in Fig. 3, the differences in the simulated wind profiles suggest that downslope wind strengths are sensitive to ambient stability; near-neutral ambient stability pro-

duces stronger jets and slightly lower jet heights, as compared with a more stable ambient atmosphere.

A question arising from the observations is how much the steep waste-rock pile immediately upwind of the gentle slope where the tethersonde observations took place contributed to the observed downslope

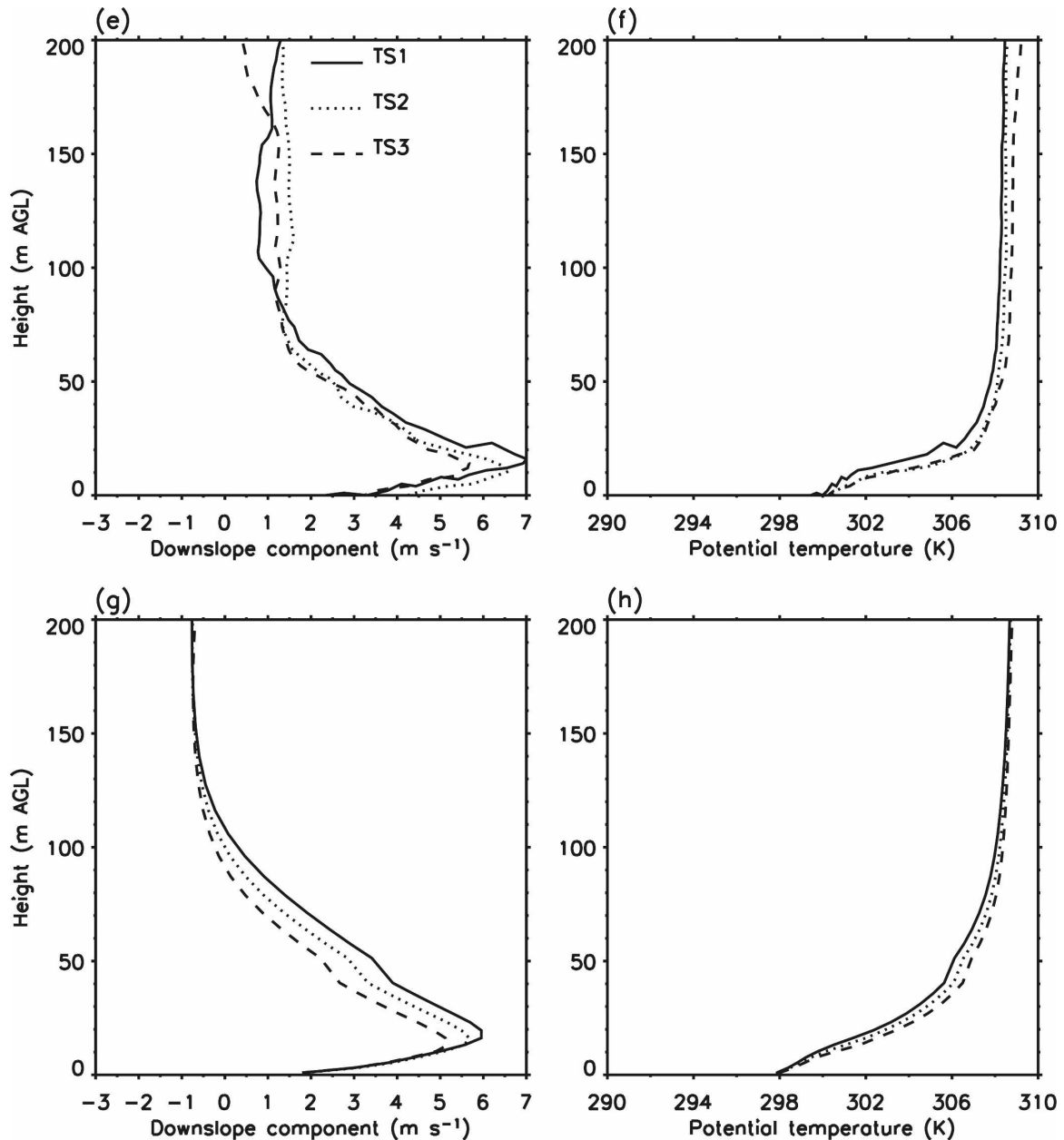


FIG. 5. (Continued)

flows and associated mass fluxes. This question can be answered by comparing the results from the simulations using terrain sections 1 and 2. Figure 7 shows the simulated downslope wind components using terrain cross section 2 for IOP 4. A comparison between Fig. 7 and Fig. 6 reveals only a small addition of the downslope wind speed attributable to the waste-rock pile, further supporting the hypothesis that the strong downslope flows observed by the tethered balloons on the gentle slope are locally produced by a temperature deficit and that the slope flow is in near-local equilibrium. How-

ever, for quantitative calculations, the waste-rock pile upwind should be included.

b. Analyses of momentum and heat balances

To understand the development of strong downslope winds over such a low-angle slope, detailed analysis of the model momentum balance equations is carried out. To obtain the momentum balance equation for the along-slope wind component, we first project the horizontal and vertical wind components to the downslope direction:

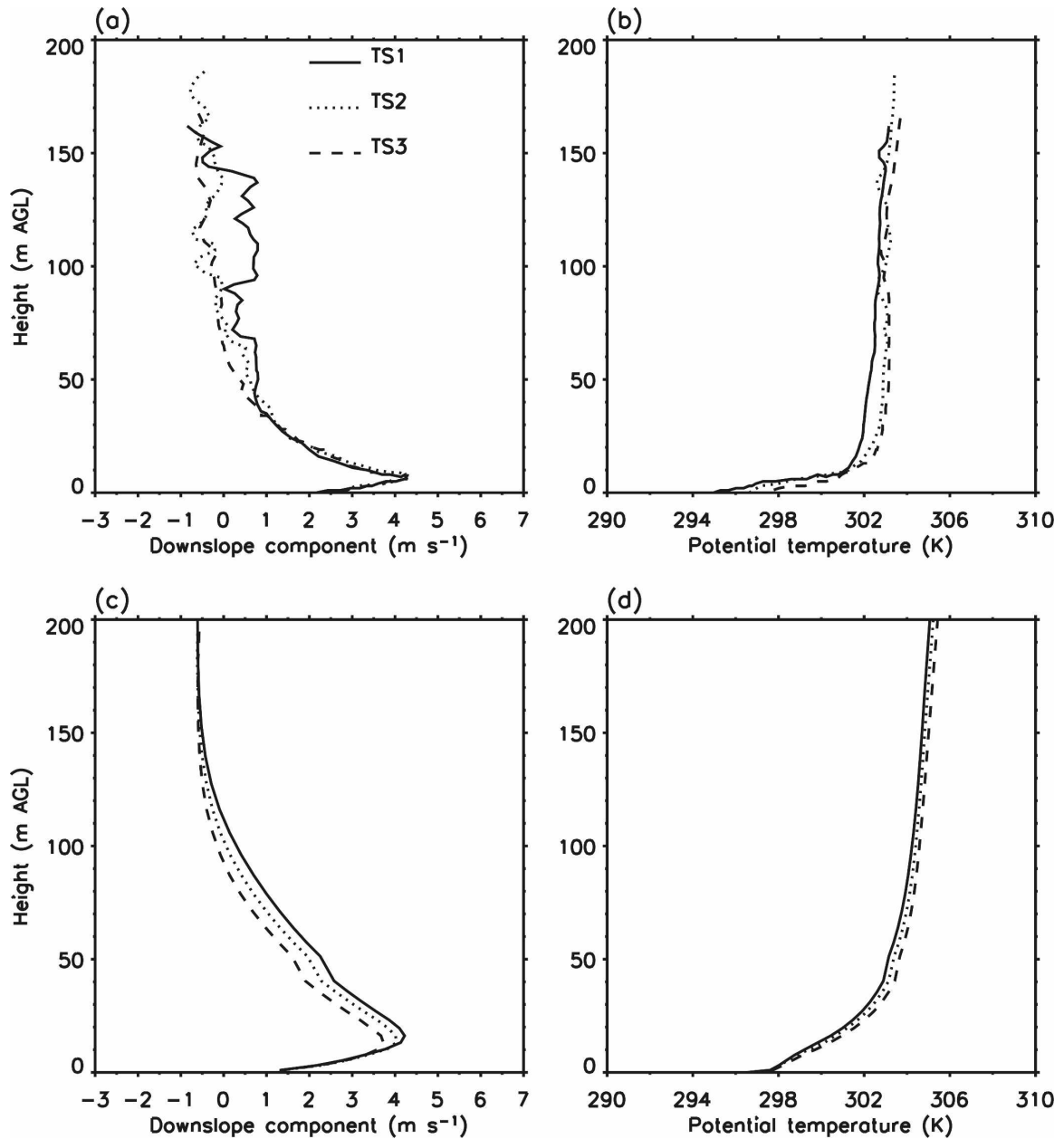


FIG. 6. As in Fig. 5, but during IOP 4 on the evening of 8 Oct 2000 at (a)–(d) 1900 and (e)–(h) 2030 MST.

$$u_s = u \cos\alpha - w \sin\alpha, \tag{1}$$

where α is the slope angle and u_s represents the down-slope wind component. The time rate of change of u_s can be obtained as

$$\frac{\partial u_s}{\partial t} = \frac{\partial u}{\partial t} \cos\alpha - \frac{\partial w}{\partial t} \sin\alpha. \tag{2}$$

The two terms $\partial u/\partial t$ and $\partial w/\partial t$ are given by the horizontal and vertical momentum equations

$$\begin{aligned} \frac{\partial u}{\partial t} = & -u \frac{\partial u}{\partial x} - w \frac{\partial u}{\partial z} - \frac{1}{\rho} \frac{\partial p'}{\partial x} + \frac{\partial}{\partial x} \left(K_x \frac{\partial u}{\partial x} \right) \\ & + \frac{\partial}{\partial y} \left(K_y \frac{\partial u}{\partial y} \right) + \frac{\partial}{\partial z} \left(K_z \frac{\partial u}{\partial z} \right) \quad \text{and} \tag{3} \end{aligned}$$

$$\begin{aligned} \frac{\partial w}{\partial t} = & -u \frac{\partial w}{\partial x} - w \frac{\partial w}{\partial z} - \frac{1}{\rho} \frac{\partial p'}{\partial z} + \frac{\partial}{\partial x} \left(K_x \frac{\partial w}{\partial x} \right) \\ & + \frac{\partial}{\partial y} \left(K_y \frac{\partial w}{\partial y} \right) + \frac{\partial}{\partial z} \left(K_z \frac{\partial w}{\partial z} \right) - g \frac{\theta'}{\theta_0}, \tag{4} \end{aligned}$$

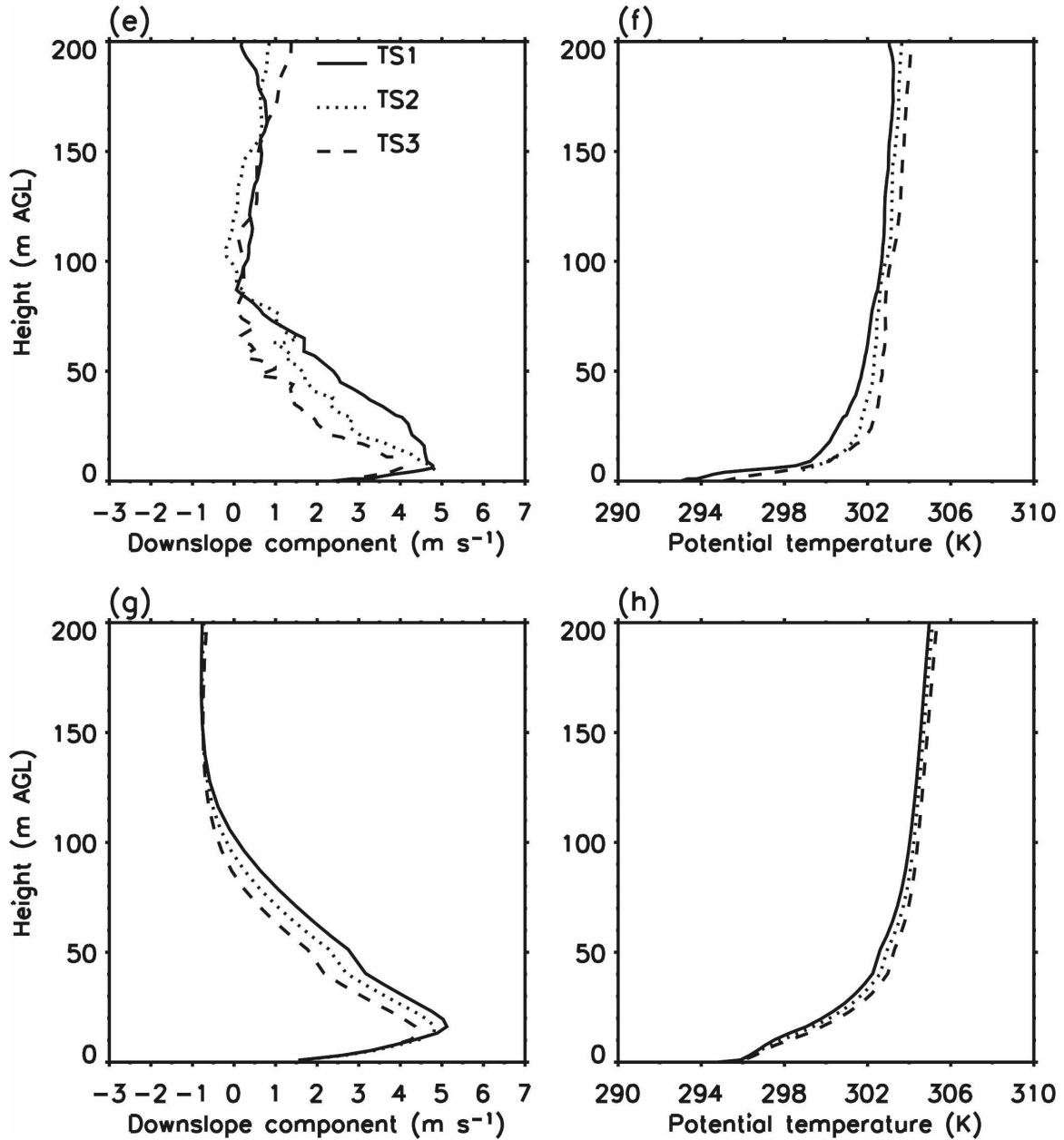


FIG. 6. (Continued)

where θ_0 and θ' are the basic state and perturbation potential temperature, respectively, and the last term in Eq.

(4) is the buoyancy force. By substituting Eqs. (3) and (4) into Eq. (2) and rearranging the terms, we obtain

$$\begin{aligned} \frac{\partial u_s}{\partial t} = & -u \frac{\partial}{\partial x} (u \cos \alpha - w \sin \alpha) - w \frac{\partial}{\partial z} (u \cos \alpha - w \sin \alpha) - \frac{1}{\rho} \left(\frac{\partial p'}{\partial x} \cos \alpha - \frac{\partial p'}{\partial z} \sin \alpha \right) + \left[\frac{\partial}{\partial x} \left(K_x \frac{\partial u}{\partial x} \right) \right. \\ & \left. + \frac{\partial}{\partial y} \left(K_y \frac{\partial u}{\partial y} \right) + \frac{\partial}{\partial z} \left(K_z \frac{\partial u}{\partial z} \right) \right] \cos \alpha - \left[\frac{\partial}{\partial x} \left(K_x \frac{\partial w}{\partial x} \right) + \frac{\partial}{\partial y} \left(K_y \frac{\partial w}{\partial y} \right) + \frac{\partial}{\partial z} \left(K_z \frac{\partial w}{\partial z} \right) \right] \sin \alpha + g \frac{\theta'}{\theta_0} \sin \alpha. \end{aligned} \quad (5)$$

By noting that $u \cos \alpha - w \sin \alpha = u_s$, Eq. (5) can be written as

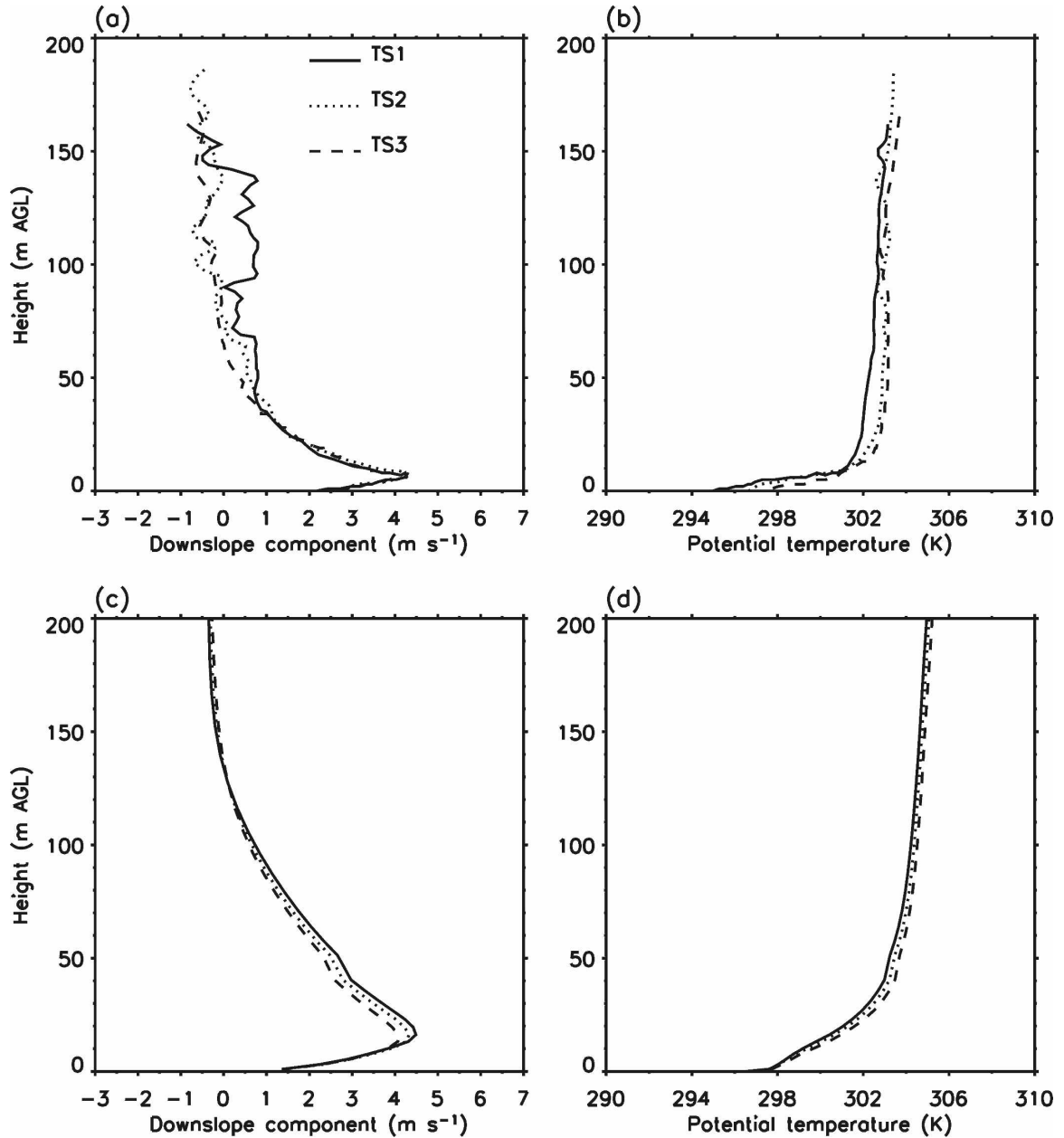


FIG. 7. As in Figs. 6a–d, but using the topography cross section in Fig. 2b.

$$\begin{aligned}
 \underbrace{\frac{\partial u_s}{\partial t}}_{\text{storage}} = & \underbrace{-u \frac{\partial u_s}{\partial x} - w \frac{\partial u_s}{\partial z}}_{\text{advection}} - \underbrace{\frac{1}{\rho} \left(\frac{\partial p'}{\partial x} \cos\alpha - \frac{\partial p'}{\partial y} \sin\alpha \right)}_{\text{pressure-gradient}} + \underbrace{g \frac{\theta'}{\theta_0} \sin\alpha}_{\text{buoyancy}} \\
 & + \underbrace{\left(\frac{\partial}{\partial x} K_x \frac{\partial u}{\partial x} + \frac{\partial}{\partial y} K_y \frac{\partial u}{\partial y} + \frac{\partial}{\partial z} K_z \frac{\partial u}{\partial z} \right)}_{\text{diffusion}} \cos\alpha - \underbrace{\left(\frac{\partial}{\partial x} K_x \frac{\partial w}{\partial x} + \frac{\partial}{\partial y} K_y \frac{\partial w}{\partial y} + \frac{\partial}{\partial z} K_z \frac{\partial w}{\partial z} \right)}_{\text{diffusion}} \sin\alpha. \tag{6}
 \end{aligned}$$

Equation (6) indicates that the time rate of change of the downslope wind speed is caused by four factors: 1) horizontal and vertical advection of the downslope wind component, 2) along-slope variation of perturba-

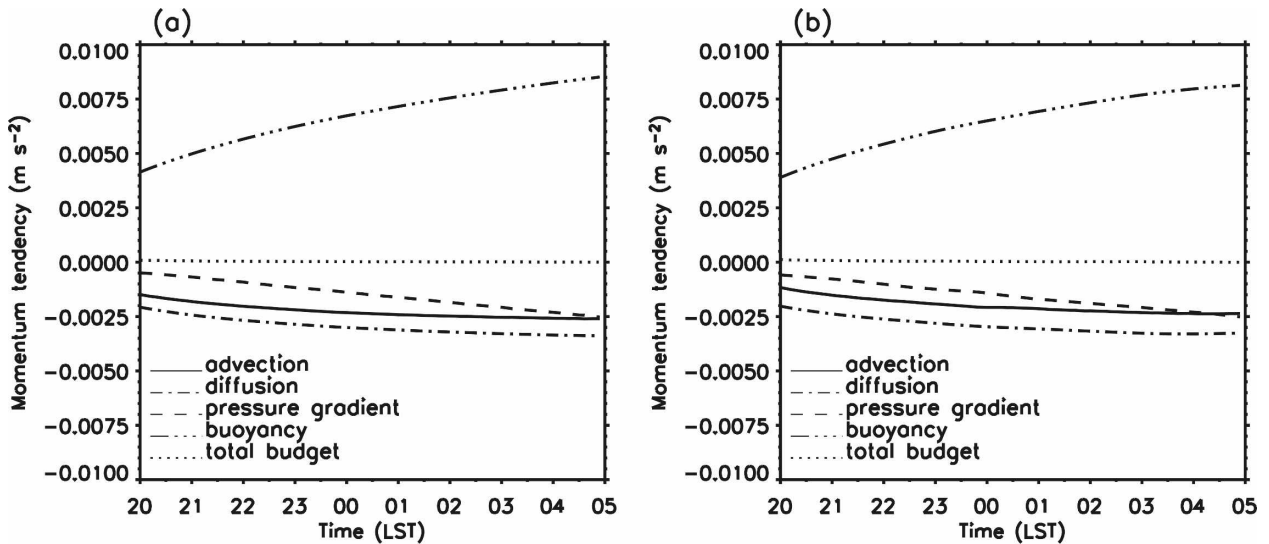


FIG. 8. Time series of the individual terms in the downslope wind momentum budget equation [Eq. (6)] averaged over the lowest 50 m at TS2 for (a) IOP 1 and (b) IOP 4.

tion pressure, 3) buoyancy, and 4) turbulent diffusion. An examination of the magnitudes and time variations of these factors would shed light on the relative importance of each of these individual forces to the initiation and evolution of the simulated downslope winds.

Figure 8 shows a time series of the individual terms in Eq. (6) averaged over the lowest 50 m at the model grid point corresponding to TS2 for IOP 1 and IOP 4. The buoyancy term, which is always positive, balances the rest of the terms that are consistently negative to produce the downslope winds. Despite the small slope angle, the buoyancy force, which is proportional to the slope angle and the perturbation potential temperature over the slope, is large enough to overcome the retardation by the other forces to produce and maintain downslope acceleration. Turbulent diffusion, as expected, retards the flow by mixing lower-momentum air aloft into the downslope-flow layer. Note that the advection term is consistently negative, suggesting that the downslope flow observed at TS2 is unlikely to be a result of advection of mass flux associated with downslope flows developed up the slope from this site; rather, it is developed locally by the small-scale temperature perturbation induced by local cooling of the slope. Another interesting aspect is that the pressure gradient force, which was previously considered to be negligible for uniform slopes (i.e., slopes with uniform slope angle and land surface characteristics), is clearly not negligible throughout the simulation.

The vertical distribution of the individual forcing terms in Eq. (6) is shown in Fig. 9 for IOP 1 and IOP 4.

Each curve represents an average over the 2-h period between 2000 and 2200 MST when the downslope winds intensified rapidly. As expected, the advection term peaks at the height of the downslope jet while both the buoyancy and turbulence diffusion terms have their maximum near the surface and decrease rapidly with height. The pressure gradient term is the smallest term at low heights, but, because it does not decrease with height as the other terms do, it becomes more important in the force balance in the upper part of the slope-flow layer.

A comparison between IOP 1 and IOP 4 in Figs. 8 and 9 provides insight into the differences in the strengths of the downslope jet developed in the two IOPs. The weaker ambient stability in IOP 1 allowed a stronger buoyancy force to develop as compared with IOP 4 when the ambient atmosphere was more stable. The larger buoyancy force yields a stronger downslope jet in IOP 1.

The vertical distribution of the heat budget terms averaged between 2000 and 2200 MST at TS2 is shown in Fig. 10 for IOP 1 and IOP 4. Figure 10 shows a positive advection term, indicating that warm-air advection associated with the downslope flow causes the local temperature at TS2 to increase. It is a common misperception that downslope winds are associated with cold-air advection. Downslope flow or drainage flow develops when air adjacent to the slope surface becomes colder than the ambient air at the same elevation and therefore sinks down the slope. This is not cold-air advection, however, because in a stable atmosphere potential temperature increases with height so

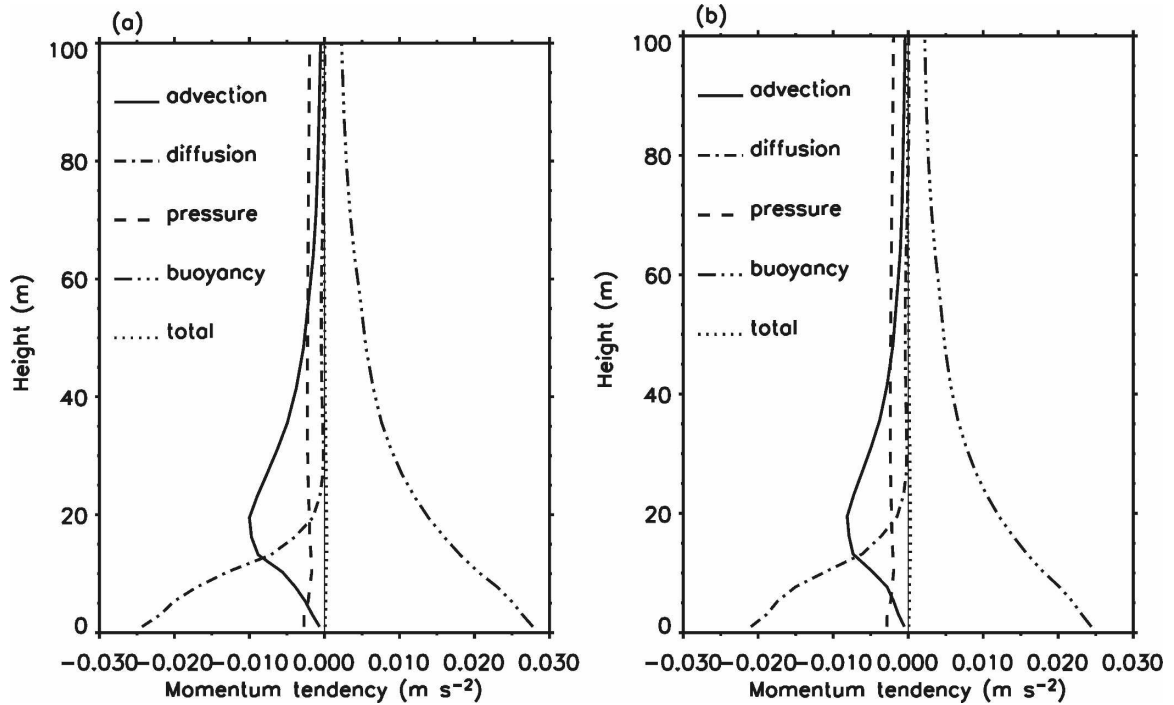


FIG. 9. Vertical distribution of the individual terms in the downslope wind momentum budget equation [(Eq. 6)] averaged for the time period 2000–2200 MST at TS2 for (a) IOP 1 and (b) IOP 4.

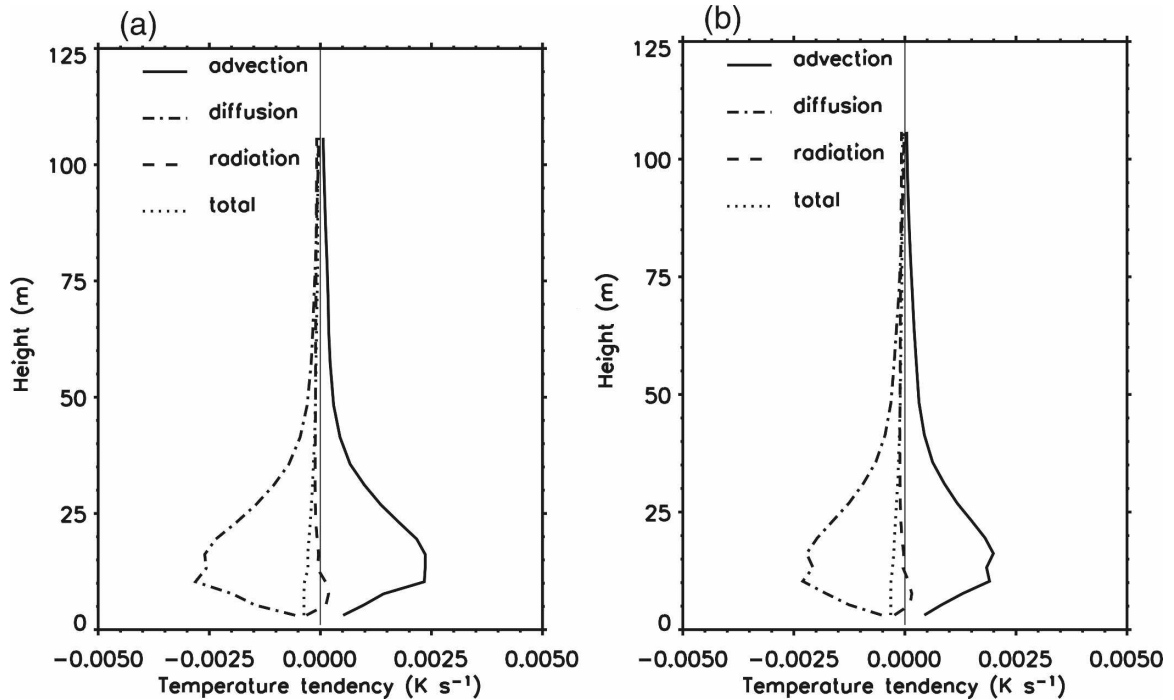


FIG. 10. Vertical distribution of the individual terms in the downslope wind heat budget equation averaged for the time period 2000–2200 MST at TS2 for (a) IOP 1 and (b) IOP 4.

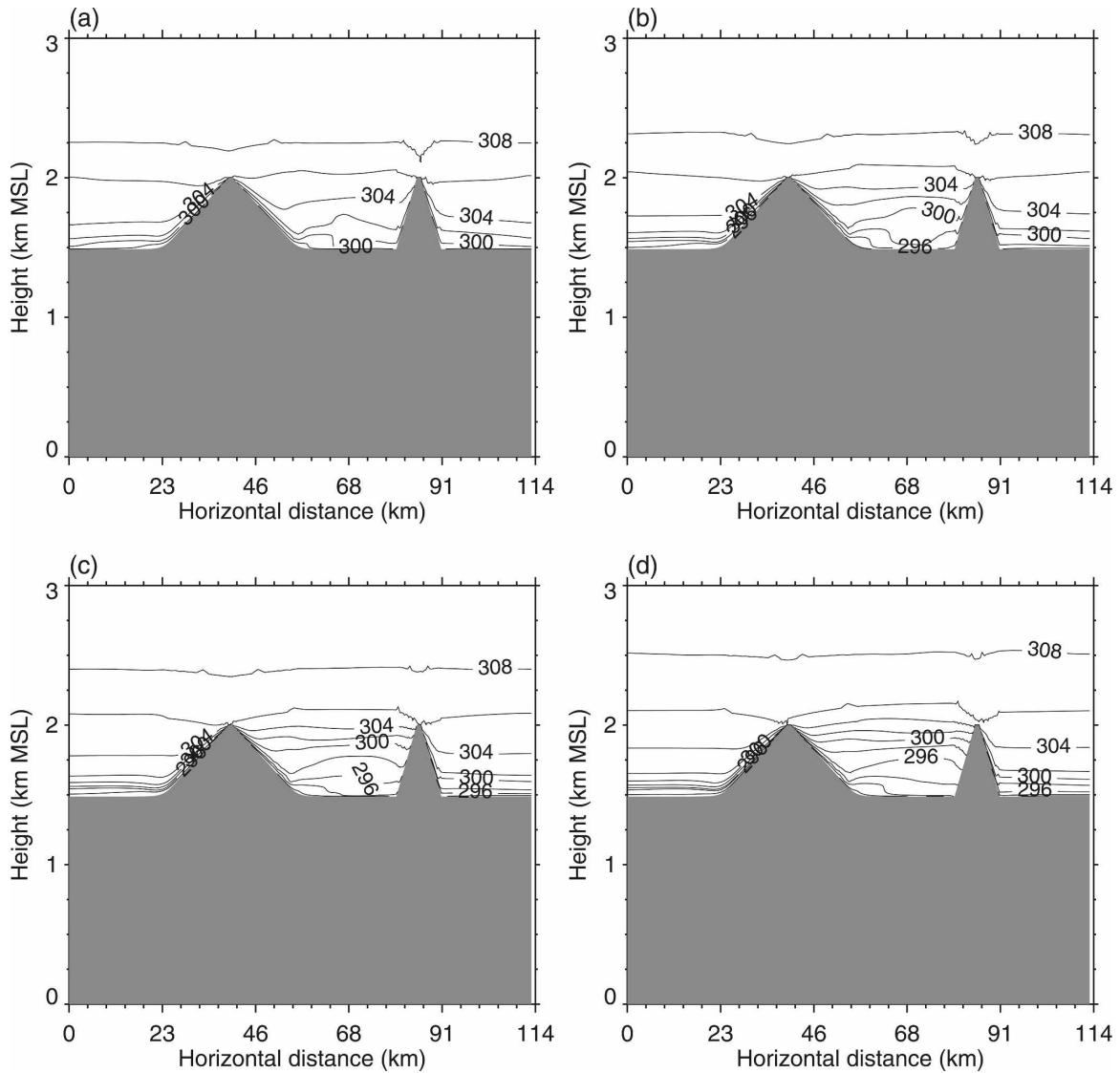


FIG. 11. The simulated potential temperature distributions on the terrain cross section in Fig. 2c at (a) 2200, (b) 0000, (c) 0200, and (d) 0400 MST.

that air at the upper slope is generally potentially warmer than the air at the lower part of the slope. Thus, when viewed from a fixed site down the slope, the advection associated with the downslope wind reaching this site is actually warm-air advection. The warm advection is usually not enough to cancel the local cooling of air adjacent to the slope as the surface of the slope continues to cool by the net loss of longwave radiation. The cold air, once reaching the bottom of a valley or basin, may accumulate to form a cold-air pool. The development of cold-air pools can affect ambient stability, which in turn may affect the evolution of downslope flows. The next section explores this aspect of slope-flow development.

c. The impact of a valley inversion

The evolution of the temperature structure and the stratification in the Salt Lake Valley has a large impact on the characteristics of the downslope flows observed by the tethersondes over the gentle slope. The simulations using the third terrain cross section are used to understand how the valley atmosphere modifies the development and evolution of downslope winds on valley sidewalls in comparison with those developed over isolated mountain slopes. In addition, the effect of the slope angle is also discussed by comparing the downslope winds over the low-angle slope with those over the steep slope.

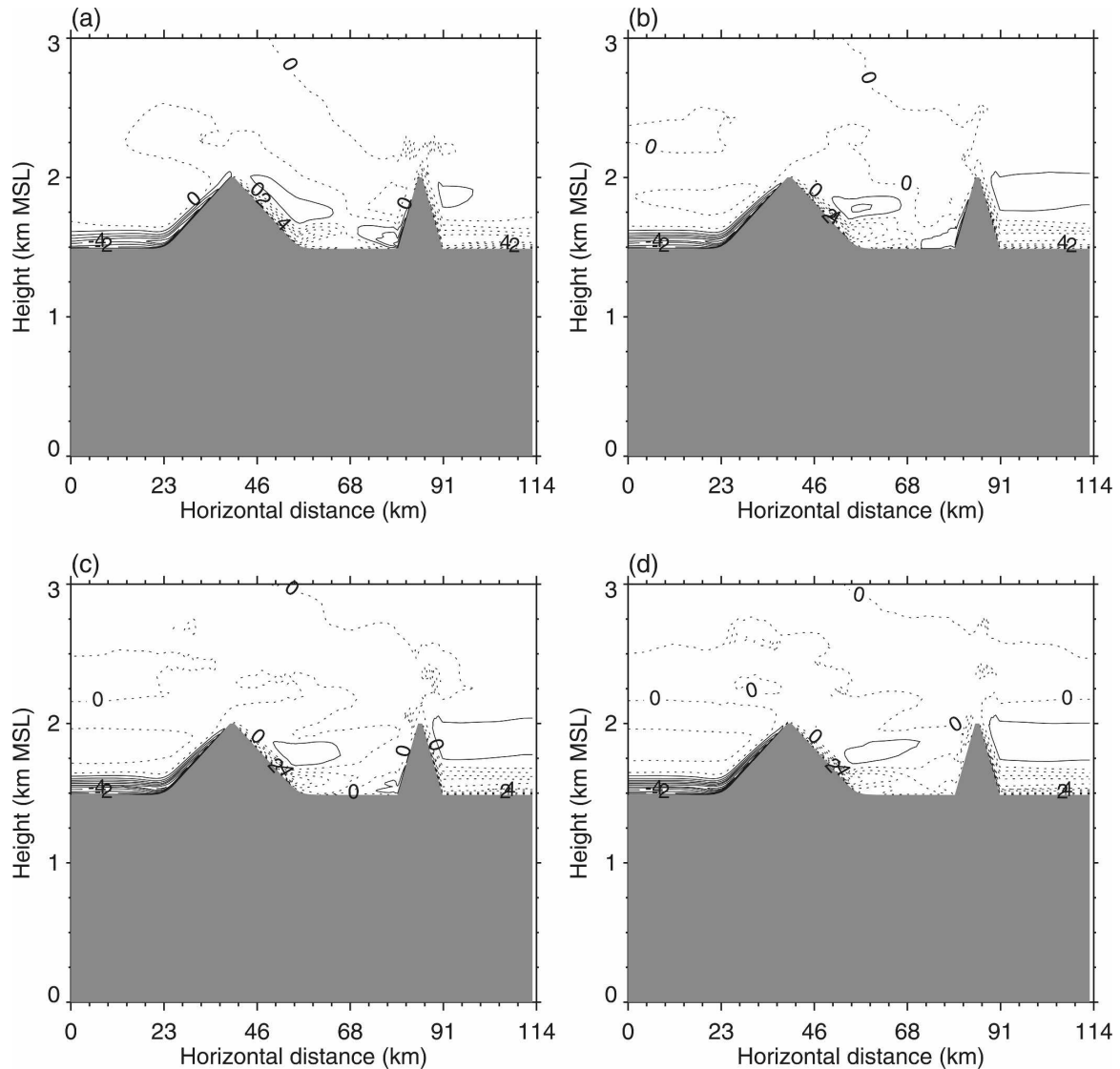


FIG. 12. The simulated u component wind speed on the terrain cross section in Fig. 2c at (a) 2200, (b) 0000, (c) 0200, and (d) 0400 MST. Solid lines are for $u < 0$, and dotted lines are for $u \geq 0$.

The simulated distribution of potential temperature and the u wind component are shown in Figs. 11 and 12 for IOP 4, the night of 8–9 October, at 2200, 0000, 0200, and 0400 MST. Outside the valley over the plain, a shallow surface-based inversion of approximately 200 m developed in the evening and continued to strengthen throughout the night. Inside the valley, the air is generally colder relative to air over the plain because of cooling of the sidewalls in addition to the cooling at the ground surface and the cold-air drainage. The cooling inside the valley, however, is distributed through a deeper layer with a weaker temperature inversion near ground but a capping inversion layer near the top of the valley atmosphere. The differences in the

temperature structure inside and outside the valley resulted in substantial differences in the development of downslope flows, which otherwise would be symmetrical about the mountain peak. Outside the valley, downslope winds increase with time; inside the valley, the deepening of the cooling in the valley reduces the horizontal temperature gradient between the valley atmosphere and the slope surface, which consequently weakens the downslope winds on the sidewalls. In addition to the difference between the inside and outside of the valley, stronger winds were found on the gentle slopes

A more quantitative comparison of the characteristics of downslope winds is given in Fig. 13, which shows

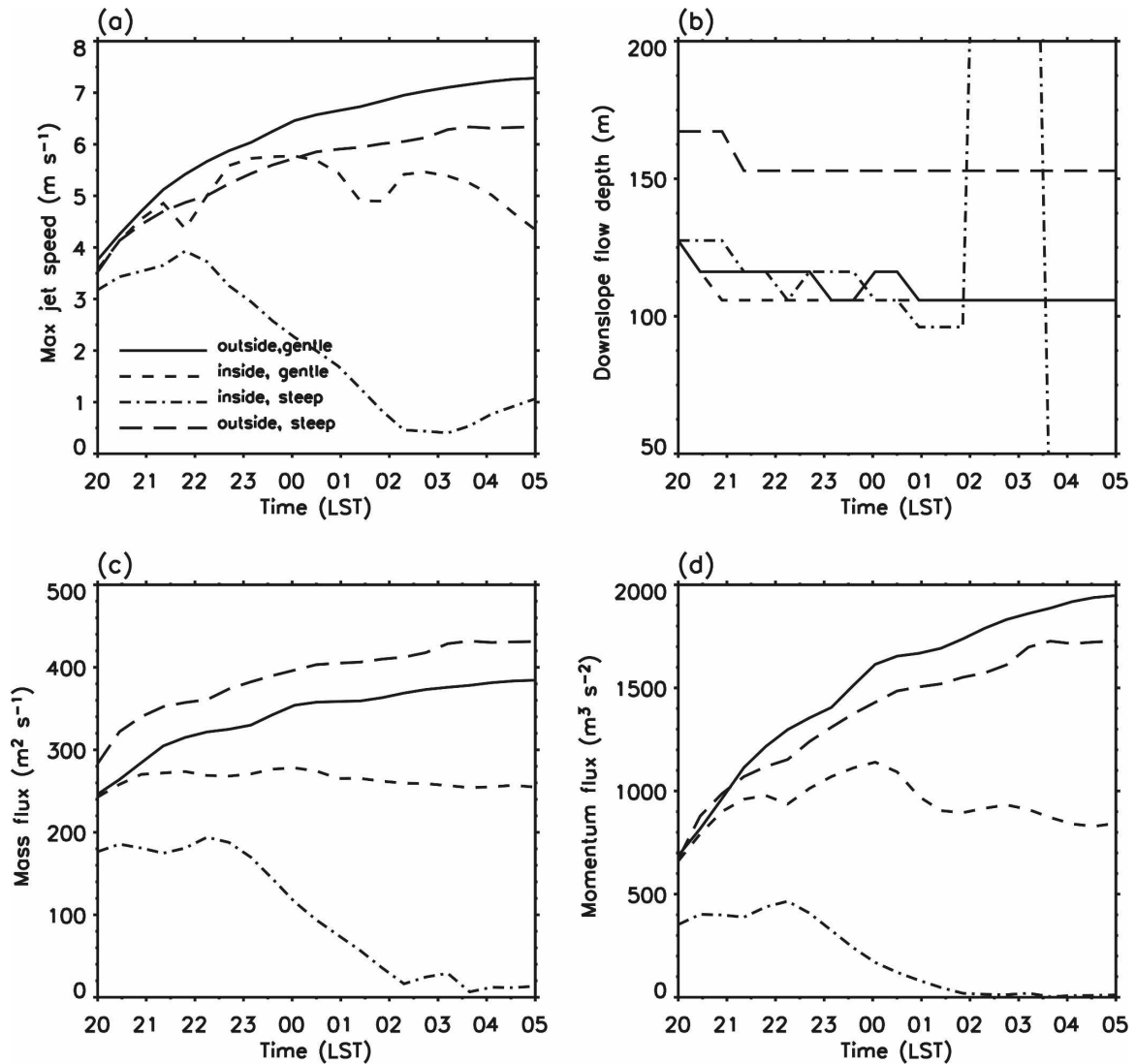


FIG. 13. The characteristics of downslope winds at the half-width point of the four slopes: (a) downslope wind maximum, (b) downslope wind depth, (c) mass flux, and (d) momentum flux.

time series of the simulated maximum downslope wind speed, the depth of the downslope wind layer, the mass flux, and the momentum flux associated with the downslope flow. For each of these properties, four curves are plotted corresponding to four locations at the mid-points of the low- and high-angle slopes both within and outside the valley. A comparison of the two curves representing the same slopes inside and outside of the valley further reveals the weakening effect of the valley temperature structure on the peak speed of the downslope flows. In addition, the downslope jet and the associated fluxes increase steadily during the course of the night outside the valley, whereas inside the valley the jet speed and the fluxes exhibit temporal oscillations. On the steep slope inside the valley, the down-

slope jet increases in the first few hours, followed by a rapid decrease and final cessation after midnight. A comparison of the properties of the downslope flows developed over the gentle slope with those above the steep slope reveals that the downslope wind is stronger above the gentle slope and deeper on the steep slope.

An examination of the momentum tendencies at the same four points can help to explain these differences in the properties of the downslope winds. As shown in Fig. 14, regardless of the slope angle and position inside or outside the valley, the momentum budget is dominated by a balance between the buoyancy force and the turbulent diffusion. The pressure gradient force, however, exhibits large variations among the four sites. The

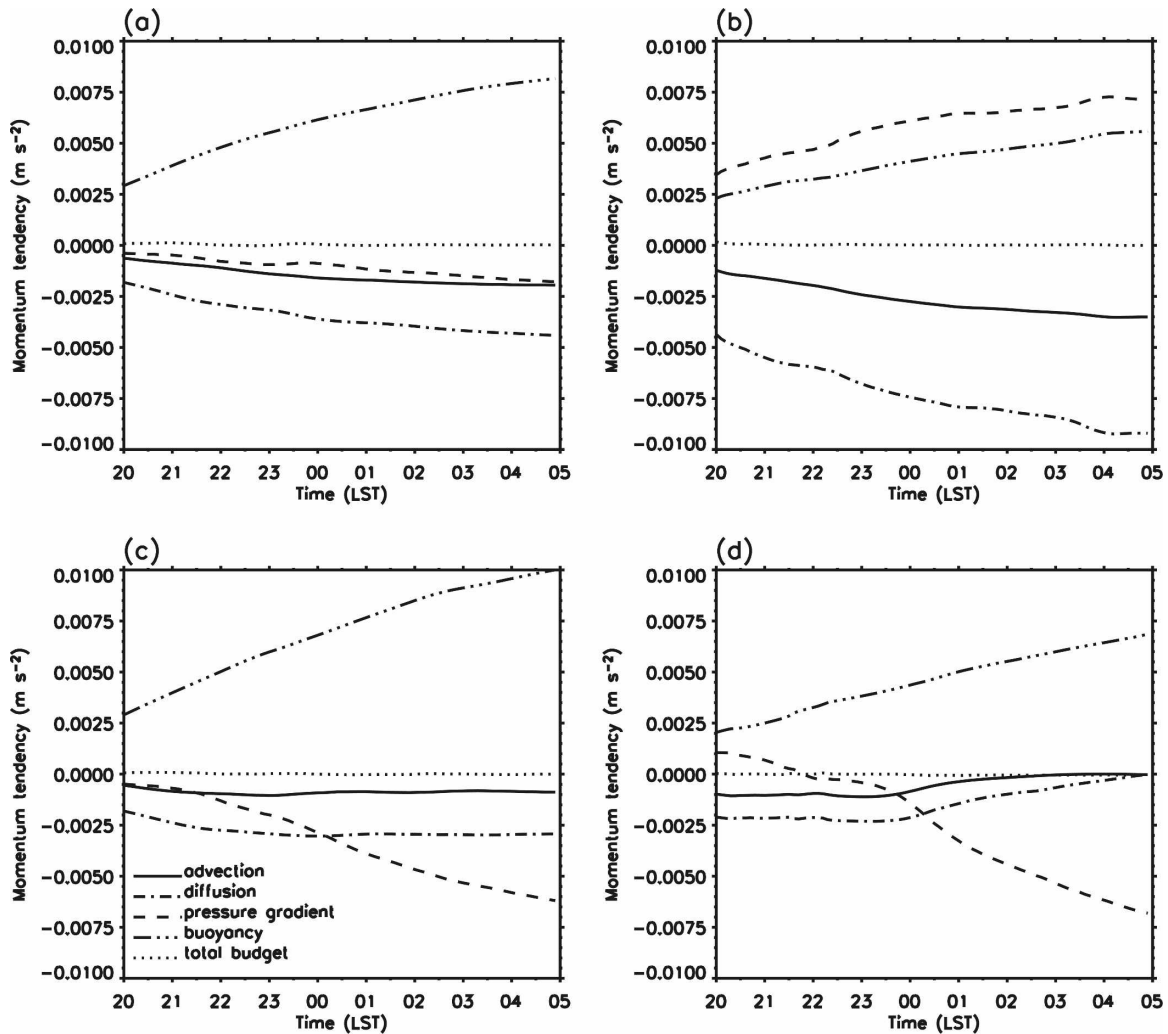


FIG. 14. Time series of the individual terms in the momentum budget equation [(Eq. 6)] at the half-width points above a (a) gentle slope on the plain side, (b) steep slope on the plain side, (c) gentle slope on the valley side, and (d) steep slope on the valley side.

values of the pressure gradient force inside and outside the valley are similar in the first few hours, but they diverge substantially afterward. Outside the valley, the pressure gradient force remains small throughout the night, whereas as the inversion builds up inside the valley the pressure gradient force increases and becomes much larger than that outside the valley later at night. This increase in the pressure gradient force tends to slow down the slope flow by partially canceling the buoyancy force that drives the flow. The increase is particularly large over the steep slope, where it eventually balances the buoyancy force and stops the slope flow. A comparison of the driving buoyancy force over the gentle and steep slopes suggests that the stronger downslope winds over the gentle slope are the result of a larger buoyancy force associated with a larger tem-

perature deficit over the gentle slope relative to that over the steep slope, as shown in Fig. 11.

d. Sensitivity to nocturnal down-valley winds and slope roughness

The observations made in the Salt Lake Valley during the VTMX experiment showed that winds in the valley are usually bidirectional, with northerly up-valley winds during the day and southerly down-valley winds at night (Doran et al. 2002). Observations also showed that although the down-valley flows occurred on most nights during the month-long experiment their strength varied from one night to another depending on synoptic-scale wind speeds and directions. To examine the impact of this along-valley wind on the develop-

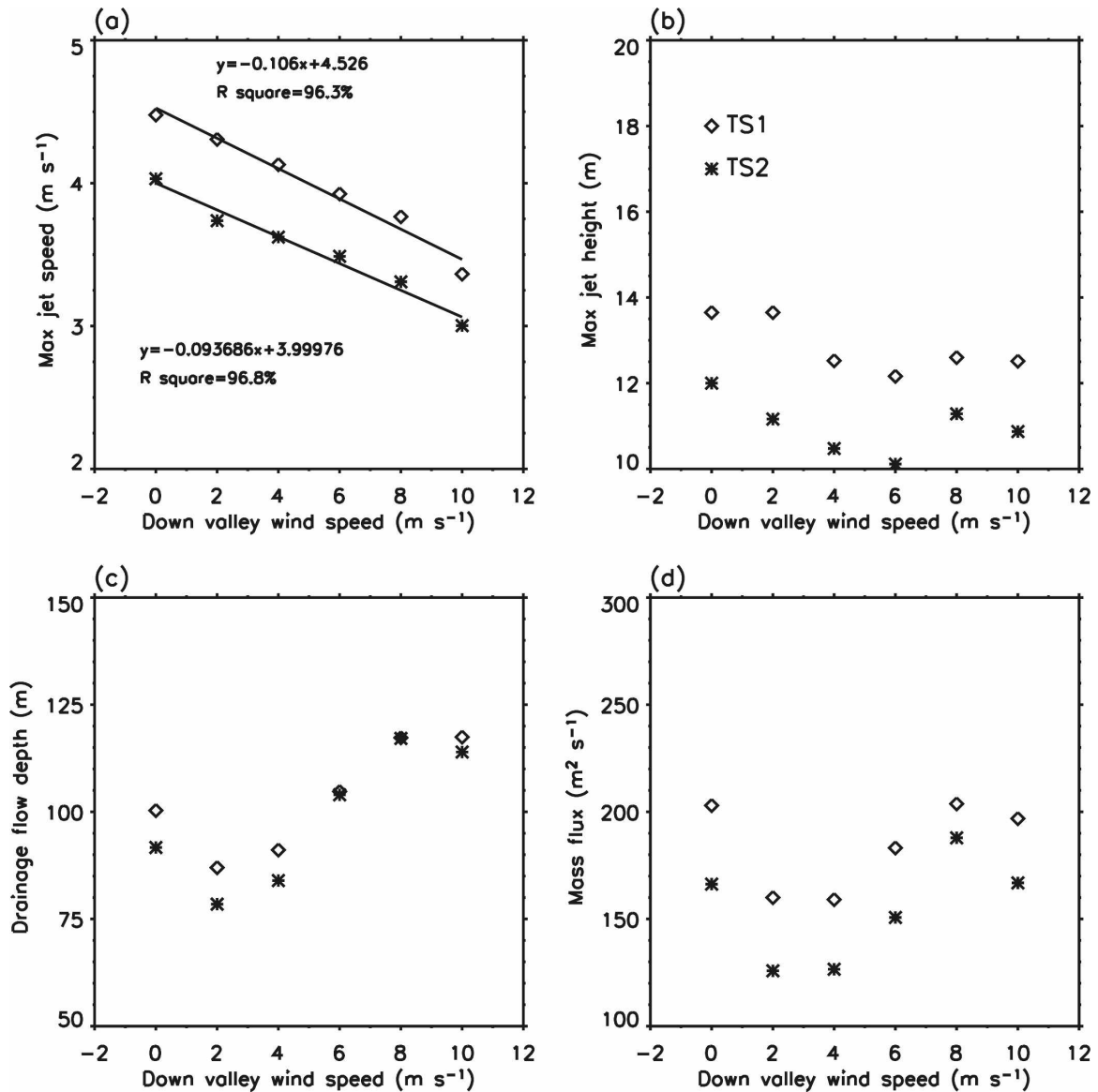


FIG. 15. Simulated slope-flow characteristics as a function of down-valley wind speed.

ment and evolution of the downslope flows, simulations were repeated for IOP 1 using the first terrain cross section, but with down-valley wind speed increasing from 0 to 10 m s⁻¹.

The resulting characteristics of the downslope winds are shown in Fig. 15. An increase in the ambient wind speed across the slope leads to an almost linear decrease in the maximum downslope jet speed but an increase in the depth of the downslope wind layer. The increase in the depth results in larger mass flux despite the weakening of the maximum wind speed. The height of the jet varies little with increasing speed of down-valley winds. These results are consistent with the findings of the Banta et al. (2004) observational study and

the Pinto et al. (2006) numerical simulations. Both of these previous studies used the actual topography of the Salt Lake Valley and focused on basinwide flows and the influence of large-scale forcing.

The sensitivity of the downslope winds to the roughness of the slope surface is also examined by repeating the simulation with the roughness length increasing from 0.05 to 50 cm. The simulated slope-flow characteristics shown in Fig. 16 reveal that the downslope wind speed is not very sensitive to an increase in roughness length. The jet height, on the other hand, is sensitive to the roughness change, with increasing slope roughness leading to a rise in the height of the downslope jet.

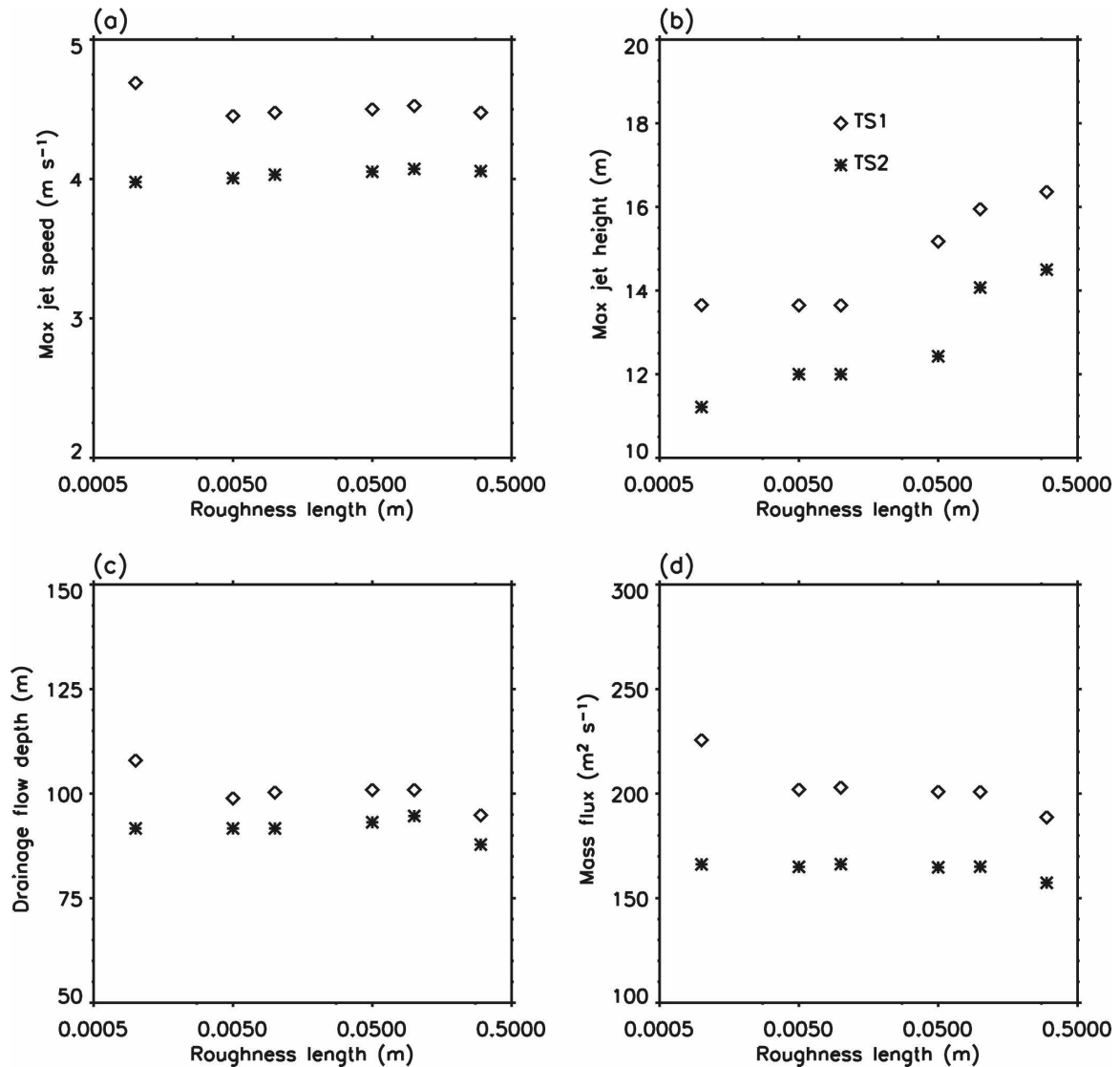


FIG. 16. Simulated slope-flow characteristics as a function of slope roughness.

5. Conclusions

Numerical simulations were performed to answer questions regarding the mechanisms responsible for the strong downslope flows observed over a 12-km-long segment of a very gentle, uniform slope on the southwestern side of the Salt Lake Valley as part of the VTMX experiment (Part I).

The results show that, despite the very low slope angle, the buoyancy force resulting from the nocturnal cooling of the slope is capable of producing a 100-m-deep downslope wind layer with maximum wind speed exceeding 6 m s^{-1} , as observed by the tethersonde soundings. There is very little contribution to the downslope mass flux from horizontal advection, which, to-

gether with the almost simultaneous appearance of a downslope wind at the four tethersonde sites, suggests that the observed downslope flow is produced locally by the temperature deficit resulting from local cooling of the slope surface.

The results also reveal that the pressure gradient force, previously considered negligible by linear theories (e.g., Mahrt 1982), can be an important term in the slope wind momentum budget. Above an isolated gentle slope, the pressure gradient force produced by the deepening of the downslope wind layer with downslope distance can partially balance the buoyancy force and therefore slow down the flow. For slopes on valley sidewalls, the pressure gradient term is most sensitive, relative to other terms in the momentum balance equa-

tion, to the buildup of the valley inversion and is responsible for the intermittency as well as the weakening/disappearing of the downslope flows.

Downslope flows are stronger over low-angle slopes than over steep slopes because of the larger buoyancy force above the lower-angle slopes. An increase in nocturnal down-valley ambient wind leads to a linear decrease in the maximum downslope wind speed and a slight deepening of slope-flow layer. Slope-flow properties are not particularly sensitive to changes in the roughness length except that the jet height increases somewhat above rougher slopes.

Acknowledgments. We thank the organizers and participants of the VTMX experiment for the use of their data and the U.S. Department of Energy (DOE) Office of Biological and Environmental Research Environmental Meteorology Program for funding the VTMX experiment and subsequent analyses. The specific contributions of the participants are listed in Part I. Our analyses were partly conducted at Pacific Northwest National Laboratory (PNNL), which is operated for DOE by Battelle Memorial Institute. Partial support was provided by the U.S. National Science Foundation by Grants ATM-0521776 (CDW) and ATM-444807 and ATM-0646206 (SZ).

REFERENCES

- Banta, R. M., L. S. Darby, J. D. Fast, J. O. Pinto, C. D. Whiteman, W. J. Shaw, and B. W. Orr, 2004: Nocturnal low-level jet in a mountain basin complex. Part I. Evolution and effects on local flows. *J. Appl. Meteor.*, **43**, 1348–1365.
- Bossert, J. E., and G. S. Poulos, 1995: A numerical investigation of mechanisms affecting drainage flows in highly complex terrain. *Theor. Appl. Climatol.*, **52**, 119–134.
- Chen, C., and W. R. Cotton, 1983: A one-dimensional simulation of stratocumulus-capped mixed layer. *Bound.-Layer Meteor.*, **25**, 289–321.
- Clements, W. E., J. A. Archuleta, and D. Hoard, 1989: Mean structure of nocturnal drainage flow in a deep valley. *J. Appl. Meteor.*, **28**, 457–462.
- Defant, F., 1949: Zur Theorie der Hangwinde, nebst Bemerkungen zur Theorie der Berg- und Talwinde. [On the theory of slope winds, along with remarks on the theory of mountain and valley winds.] *Arch. Meteor. Geophys. Bioklimatol.*, **A1**, 421–450. [English translation: Whiteman, C. D., and E. Dreiseitl, 1984: Alpine meteorology: Translations of classic contributions by A. Wagner, E. Ekhardt and F. Defant. PNL-5141/ASCOT-84-3. Pacific Northwest Laboratory, Richland, Washington, 121 pp.]
- Doran, J. C., and T. W. Horst, 1981: Velocity and temperature oscillations in drainage winds. *J. Appl. Meteor.*, **20**, 361–364.
- , J. D. Fast, and J. Horel, 2002: The VTMX 2000 campaign. *Bull. Amer. Meteor. Soc.*, **83**, 537–551.
- Fitzjarrald, D. R., 1984: Katabatic wind in opposing flow. *J. Atmos. Sci.*, **41**, 1143–1158.
- Fleagle, R. G., 1950: A theory of air drainage. *J. Meteor.*, **7**, 227–232.
- Gutman, L. N., 1983: On the theory of the katabatic slope wind. *Tellus*, **35A**, 213–218.
- Haiden, T., and C. D. Whiteman, 2005: Katabatic flow mechanisms on a low-angle slope. *J. Appl. Meteor.*, **44**, 113–126.
- Hunt, J. C. R., H. J. S. Fernando, and M. Princevac, 2003: Unsteadily thermally driven flows on gentle slopes. *J. Atmos. Sci.*, **60**, 2169–2182.
- Kondo, J., and T. Sato, 1988: A simple model of drainage flow on a slope. *Bound.-Layer Meteor.*, **43**, 103–123.
- Louis, J.-F., 1979: A parametric model for vertical eddy fluxes in the atmosphere. *Bound.-Layer Meteor.*, **17**, 187–202.
- Mahrt, L., 1982: Momentum balance of gravity flows. *J. Atmos. Sci.*, **39**, 2701–2711.
- , D. Vickers, R. Nakamura, M. R. Soler, J. Sun, S. Burn, and D. H. Lenschow, 2001: Shallow drainage flows. *Bound.-Layer Meteor.*, **101**, 243–260.
- Manins, P. C., and B. L. Sawford, 1979a: A model of katabatic winds. *J. Atmos. Sci.*, **36**, 619–630.
- , and —, 1979b: Katabatic winds: A field case study. *Quart. J. Roy. Meteor. Soc.*, **105**, 1011–1025.
- McNider, R. T., and R. A. Pielke, 1984: Numerical simulations of slope and mountain flows. *J. Appl. Meteor.*, **23**, 1441–1453.
- Mellor, G. L., and T. Yamada, 1982: Development of turbulence closure model for geophysical fluid problems. *Rev. Geophys.*, **20**, 851–875.
- Monti, P., H. J. S. Fernando, M. Princevac, W. C. Chan, T. A. Kowalewski, and E. R. Pardyjak, 2002: Observations of flow and turbulence in the nocturnal boundary layer over a slope. *J. Atmos. Sci.*, **59**, 2513–2534.
- Orgill, M. M., and R. I. Schreck, 1985: An overview of the ASCOT multi-laboratory field experiments in relation to drainage winds and ambient flow. *Bull. Amer. Meteor. Soc.*, **66**, 1263–1277.
- Petkovsek, Z., and A. Hocevar, 1971: Night drainage winds. *Arch. Meteor. Geophys. Bioklimatol.*, **20A**, 353–360.
- Pielke, R. A., and Coauthors, 1992: A comprehensive meteorological modeling system—RAMS. *Meteor. Atmos. Phys.*, **49**, 69–91.
- Pinto, J. O., D. B. Parsons, W. O. J. Brown, S. Cohn, N. Chamberlain, and B. Morley, 2006: Coevolution of down-valley flow and the nocturnal boundary layer in complex terrain. *J. Appl. Meteor. Climatol.*, **45**, 1429–1449.
- Poulos, G. S., 1997: The interaction of katabatic winds and mountain waves. Ph.D. dissertation, Colorado State University, 297 pp. [Available as Publication LA-13224-T from Los Alamos National Laboratory, Los Alamos, NM 87545.]
- Skyllingstad, E. D., 2003: Large-eddy simulation of katabatic flows. *Bound.-Layer Meteor.*, **106**, 217–243.
- Smith, C. M., and E. D. Skillingstad, 2005: Numerical simulation of katabatic flow with changing slope angle. *Mon. Wea. Rev.*, **133**, 3065–3080.
- Tremback, C. J., and R. Kessler, 1985: A surface temperature and moisture parameterization for use in mesoscale numerical models. Preprints, *Seventh Conf. on Numerical Weather Prediction*, Montreal, QC, Canada, Amer. Meteor. Soc., 355–358.
- Whiteman, C. D., and S. Zhong, 2008: Downslope flows on a low-angle slope and their interactions with valley inversions. Part I: Observations. *J. Appl. Meteor. Climatol.*, **47**, 2023–2038.
- , —, W. J. Shaw, J. M. Hubbe, X. Bian, and J. Mittelstadt, 2001: Cold pools in the Columbia basin. *Wea. Forecasting*, **16**, 432–447.
- Zhong, S., and J. Fast, 2003: An evaluation of the MM5, RAMS, and the Meso-Eta models at subkilometer resolution using the VTMX field campaign data in the Salt Lake Valley. *Mon. Wea. Rev.*, **131**, 1301–1322.